Modelling conduction delays in the corpus callosum using MRI-measured g-ratio

Berman S.[1], Filo S. , Mezer A. A.

1. Edmond & Lily Safra Center for Brain Sciences, The Hebrew University of Jerusalem, Jerusalem, Israel

Abstract

Conduction of action potentials along myelinated axons is affected by its structural features, such as the axonal g-ratio. The g-ratio is the ratio between the inner and outer diameters of the myelin sheath surrounding the axon. The effect of g-ratio variance on conduction properties has been quantitatively evaluated using single-axon models. It has recently become possible to estimate a g-ratio weighted measurement using quantitative MRI. Nevertheless, it is still unclear whether the variance in the g-ratio in the healthy human brain leads to significant differences in conduction velocity. In this work we tested whether the g-ratio MRI measurement can be used to predict conduction delays in the corpus callosum.

We present a novel framework in which the structural properties of fibers (i.e. length and g-ratio, measured with MRI), are incorporated in a biophysical model of axon conduction, to predict conduction delays of long-range white matter fibers. We applied this framework to the corpus callosum, and found conduction delay estimates that are compatible with values generated more directly (~15 ms).

Furthermore, since studies that use response time and electrophysiology suggest an increase in conduction delays with age, we compared younger and older subjects. We investigated whether there are differences in the g-ratio and the fiber length between the age groups, and whether they lead to a difference in conduction delays. We found no significant differences between the predicted delays of the two groups.

Our study provides a framework for predicting conduction latencies *in vivo*. The framework could have major implications for future studies of white matter diseases and large range network computations. Our results highlight the need for improving additional *in vivo* measurements of white matter microstructure.

1. Introduction

White matter tissue consists of myelinated and non-myelinated axons and glial cells. These axons form large-scale networks which are necessary for learning (1–3), cognitive functions (4), and normal development, and normal aging (5,6). Furthermore, damage to the structure of the white matter has been associated with a variety of diseases and disorders, including multiple sclerosis and schizophrenia (7,8). These networks of white matter fibers are essential for brain function because their main role is to conduct action potentials between distant brain regions. The conduction delays along white matter fibers could have computational implications and they were shown to vary with many factors, including age (9), sex (10), and various medical conditions (11).

In vivo anatomical studies of white matter often use indirect measures of its structure and integrity properties, leaving a gap in the interpretation of their results (12–14). Nevertheless, *ex vivo* and *in vitro* studies have led to a rich understanding of the biophysical connection between the axon microstructure and its conduction properties (e.g., (15–17)). Moreover, computational models of conduction of action potentials along myelinated axons provide a way to explore the dependence of the conduction properties on the axons' geometrical and electrical properties.

One such geometrical property of axons, which has been the focus of various studies, is the g-ratio. The g-ratio (g) is the ratio between the inner and outer diameters of the myelin sheath surrounding the axon. For a fixed inner diameter (axon diameter, d), changing g means changing the myelin sheath thickness, thus affecting membrane resistance and capacitance. For a fixed outer diameter (fiber diameter, D), changing g means varying both myelin sheath thickness and intra-axonal space, thus affecting axial conductivity as well. Under these assumptions Rushton found analytically that an optimal g for conduction velocity is around 0.6 (18). Further work has shown that higher values would be optimal given other parameters of the tissue such as energy consumption or volume constraints (19).

Empirical values of g-ratio can be measured directly using invasive techniques such as electron microscopy. Such studies reveal the g is indeed distributed around near optimal values: the reported values are around 0.67 for monkey's corpus callosum (20,21), 0.81 for guinea pigs' optic nerve (22), 0.76 for the mouse corpus callosum (23) and 0.75-0.8 for the rat corpus callosum (24). It has recently become possible to estimate a g-weighted measurement in humans *in vivo* using quantitative MRI (qMRI) (25–29). These measurements provide values and trends that are similar to those found with histology (21,27). Nevertheless, it is unclear whether the variance captured by the *in vivo* g measurements in the healthy human brain can be translated to meaningful differences in conduction velocity.

In this work we tested whether the g-weighted MRI measurement can be used to account for conduction delays in the corpus callosum. Theoretical estimates of conduction time across the callosum have been previously used in cross-species studies (30). Callosal delays can be estimated *in vivo* using electrical recordings such as EEG or MEG, and have been shown to be related to callosal structure (31,32), and are likely to increase with age (33,34). This increase could be related to white matter structure, since it's been shown that the brain tissue structure changes with age, with accumulating damage to the white matter (35,36). The structure-function link in white matter was also shown in a recent study that found correlations between callosal delays, measured using EEG, and axon diameter distributions measured using MRI (32).

To test whether the g-weighted MRI measurements can be used to predict callosal delays, we first discuss a theoretical model that can be used to calculate conduction velocity for a single axon. Next, we describe how we implement this model to calculate conduction delays in the corpus callosum. Finally, we use the framework to estimate conduction in both younger (under 40) and older subjects (over 65). Thus, we test whether incorporating the g-weighted MRI measurement in a biophysical model of conduction allows us to predict the previously observed increase in delay as function of age.

2. Theory – predicting conduction latencies

In the theory section we propose a framework that relates MRI measurements of averages of microstructure features to single axon conduction models, in order to predict white matter conduction *in vivo* (EEG/MEG). For this purpose, we first identify a relevant axon model, and the essential parameters in the model (section 2.1). Then, we describe the available qMRI parameters that can be used to estimate those model parameters (section 2.2). For model parameters that cannot be estimated based on qMRI measurements, specific values must be assumed. We will describe the assumptions underlying the choice of specific values for those parameters (section 2.3). In this section we also discuss how these parameters can be applied to a model for predicting conduction along a certain tract.

2.1 Conduction in myelinated axons

The myelinated fiber is comprised of two qualitatively different sections: the nodes of Ranvier and the internodes. The nodes of Ranvier, which contain a high density of voltage-gated Na+ channels can generate action potentials. The internodes are long sections between the nodes (about 10^3 longer), and they are coated by many layers of myelin sheaths (37). Due to the myelin sheath, the voltage progression in the internode can be described as passive. The progression of voltage along both segments of the axons have already been modelled and numerically simulated (e.g., 12,24–26). This understanding of the axon signal conduction, together with knowledge on the axon's

electrical properties (41,42) and the ability to measure its geometry, will allow to implement a model that links white matter structure with function in biophysical terms.

2.1.1 Dependence of conduction velocity on axon geometry

The determinants of conduction velocity of action potential propagation along a myelinated axon have been previously described and modelled. Rushton (18) was the first to describe the dependence of the conduction velocity of a myelinated axon on its geometry. Rushton showed that for a myelinated axon, the conduction velocity (θ) is proportional to internode length (l). The internode length, in turn, is roughly proportional to the fiber diameter (D), which can be defined using the axon diameter (d) and the g-ratio (g): $D = d/g$. According to his formulation, we could predict conduction velocity, up to a proportionality factor, using the axon diameter and g (equation 1):

$$\theta \propto l \propto Dg\sqrt{-ln(g)} \propto d\sqrt{-ln(g)} \quad (1)$$

Rushton's formulation provides an expression proportional to conduction velocity. Following studies have replicated Rushton's predictions and shown the dependence of the axon's conduction velocity on its diameter, internode length, and myelin sheath thickness (43–46). Others studies evaluated the effect of additional parameters of the axon on conduction velocity. For example, Moore et al. (38), using numerical simulations of myelinated fibers, examined both geometrical and physiological parameters. The simulations replicated the results showing a dependence of conduction velocity on internode properties, while also revealing that node parameters have a minimal effect on the conduction velocity.

Moore's approach of numerically simulating the voltage propagation, provides a direct approximation of conduction velocity, and allows a 'direct' manipulation of the different axon properties, which could be useful for the purpose of this study. In this study we use a recent MATLAB implementation by Lorena et al. (47) that numerically simulates the conduction along a myelinated axon using the formalization of Halter and Clark's model (39). Specifically, the simulation models the axon by dividing it into compartments representing the node, paranode and internode. For each time step, current flows are calculated. The current flows across the membrane (either the axonal membrane or the total myelin membrane) is calculated from the values of voltage, voltage change rate, and the specific membrane capacitance and conductances. The intracellular and periaxonal axial current flow are calculated from the specific intracellular or periaxonal resistance and the gradient of intracellular or periaxonal voltage.

2.2. The measurements in qMRI

Using a biophysical model such as the simulation used here, allows for the computation of the conduction time of an action potential along a "theoretical axon", which represents an average axon in an axonal fascicle. In order to do so *in vivo*, we should be able to measure white matter pathways and estimate their microstructure. In particular, in the section below we describe ways to measure the necessary geometrical measurements: the axon diameter, g, and axon length. In the following subsections, we describe recent

advances in qMRI, which allow for ongoing improvement in estimating the axon diameter, the g-ratio and the overall tract length.

2.2.1 Diffusion and axon properties

Diffusion MRI (dMRI) provides an important tool for measuring white matter microstructure *in vivo*. Water molecules impinge on cellular membranes, intracellular organelles, neurofilaments, and myelin. The diffusion displacement distribution therefore contains information about all of these structures. When the diffusion is measured in different directions, models can be applied to the data, and these models' parameters can be used to represent the white matter microstructure (48).

Axon diameter. There are several methods of acquiring and modelling dMRI to measure the mean axon diameter or the axon diameter distribution. Currently most of the methods are challenging since they require multi-shell high angular resolution diffusion imaging (HARDI) data, special diffusion acquisition sequences (e.g. oscillation gradients), and/or knowledge of the main orientation of fibers. Furthermore, current methods have a limited sensitivity for small axons (49), and some controversy remains regarding the feasibility of these measurements (50). While these limitations make *in vivo* measurement of axon diameter challenging, the existing methods have been validated using histology and phantoms (e.g., 24,52,53).

g-ratio. The voxel average g-ratio may be estimated using a model combining dMRI parameters reflecting axon or fiber volume in the voxel (Fiber Volume Fraction, FVF), with an MRI-myelin measurement (Myelin Volume fraction, MVF) (25). The dMRI models that were previously used to calculate g-ratio include NODDI (21,54), ActiveAx (28,55), TFD (29,56), and tensor modeling (25,57,58). The MVF also saw several implementations including mcDesspot (26,59), multiExp T2 (60–62), T2* (63,64), qMT (25,29,57,62,65–68), and non-water fraction (27,28,69). Each measure has its own advantages and disadvantages, and the choice of more specific measurements often comes with a reduced signal to noise ratio (SNR). Recent work compared the reliability of several of the different g-ratio methods and found NODDI to be more reliable than FA for the FVF estimation, where MTV and qMT were similar, with qMT having some advantage (70).

Length. Tractography algorithms use dMRI to reconstruct the white matter fiber tracts (71,72). The tract reconstruction provides the pathway length which is a critical parameter for measuring conduction time (rather than velocity).

Tract properties. Since this work aims at assessing conduction in white matter, it is necessary to characterize the white matter microstructure belonging to specific relevant white matter fibers. Using tractography it is possible to measure structural MRI measurements (g, d), along the reconstructed white matter tracts, either along the core (i.e. the mean position of the streamlines' position per node) , per voxel, or per streamline (71,73,74). An example of such measurement within a single subject is shown in figure 1:

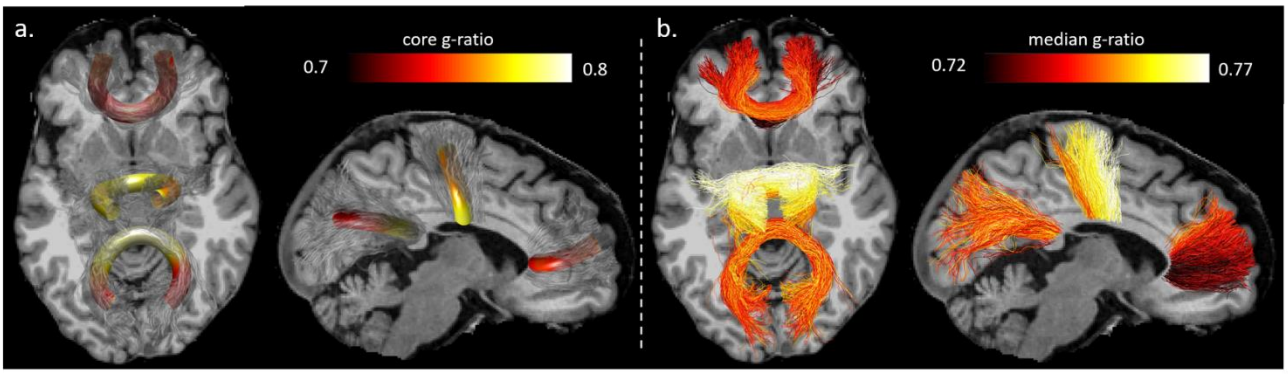

Figure 1: sampling g-ratio along a fiber tract. a. g-ratio values of 3 callosal tracts, of a single subject. The g-ratio can be calculated for **a**. the tract core, or **b.** for each streamline separately. The two methods were both calculated using AFQ (67), and they sample the space differently. While the range of values is somewhat smaller in the streamline space, it is clear in both methods that there is a difference between the different tracts.

2.2.2 Modelling Local Field Potential (LFP) from MRI data

Having performed tractography, and measuring g-ratio and axon diameter along relevant fiber tracts, one can then use these measurements in the axon model and predict the mean conduction time for an individual or groups of subjects. Additional analysis of the data might reveal more about conduction properties. For example, one can use the variance of estimated latencies within a single subject's white matter tract, and try to model the entire ERP (and not just its peak or onset). The framework implemented in a recent study (75) allowed for a simplistic model that simulates LFP measures (from MRI structure). Modelling an LFP from the MRI data allows for a more comprehensive comparison with the electrical signal: ERP width, amplitude etc. While these properties are likely to be also affected by cortical processing as well as skull shape and thickness, it is worth testing the extent to which the white matter contributes to the recorded electrical signal.

2.3. Simulation and choice of parameters

To use a model of axon conduction, we first need to choose and fix several of the model parameters that cannot be measured with MRI. These parameters include the axon geometry, and specific electrical properties of the axon (e.g. specific axial resistance). Importantly, the axon's specific electrical properties have been measured in rodents and primates and are considered to be conserved over species (42). Nevertheless, exceptions are possible, as evident from a recent study which found that the human membrane capacitance is 0.45 $\mu F/cm^2$ and not 0.9 as is the case with mice (76).

While the electrical properties of the axon are thought to be conserved, the geometrical aspects have been shown to vary with age, disease, and possibly with learning and behavior. Therefore, a clear limitation in modeling the human white matter conduction time is that not all geometrical parameters can be measured *in vivo*. These parameters will have to be assumed, based on the literature. The internode length, for example, is a significant parameter (44,77–79), yet the MRI resolution and measurements, do not

allow such information to be extracted. Fortunately, many geometrical properties of the axon share a close to linear relationship: It has been shown that g can be described as a monotonic function of the axon diameter, and that the internode length is roughly a linear function of the axon diameter (16,24,80,81). The latter relationship was used to reach Rushton's formulation, and it can be used explicitly when assuming an internode length for the simulation.

We explored the conduction velocity as calculated with the simulation, for a range of values for axon diameter (d) and fiber diameter (D)). We chose values that were found for myelinated axon in the human central nervous system (82), with values ranging from 0.2 to 5 μm for both d and D The internode length was calculated as a linear function of the fiber diameter, as found in the anterior medullary velum of the adult rat : $L = 117 + 30 \cdot D$ (83). The specific membrane capacitance was set to 0.45 $\mu F/cm^2$ (76). The rest of the (electrical) properties were fixed as described in table 1 of Lorena et al,'s paper (40). It can be seen in Figure 2a that the larger the fiber diameter (D), the faster it will conduct. Furthermore, for a given fiber diameter, the conduction velocity as a function of axon diameter (d) has a maximum around g=0.6, as shown by Rushton. This result is not surprising: given a constant fiber diameter, dramatically decreasing g means a very small axon diameter, thus reducing intra-axonal conductivity, while increasing g will reduce the leak resistance (42).

In the simulation described above, we varied the g-ratio and the axon diameter. However, since in our MRI dataset (as in many others) we cannot calculate an estimate of axon diameter, we test whether measuring g alone will be meaningful. To calculate conduction velocity with no estimate of axon diameter, we must first choose and fix the axon diameter for all tracts and subjects. The choice of axon diameter should be informed by known histological measurements. Aboitiz (82) showed the corpus callosum axon diameter distribution in the human brain is mostly centered around values close to 1, with very few axons as large as 5 microns in diameter. A weighted average of the distributions (weighted by axon diameter to give more weight to larger diameters), is closer to 2 microns, and might be closer to what the volume-sensitive MRI estimates capture in the g-ratio estimation (84).

Figure 2b shows the predicted velocities of axons with a radius of 1, 2 or 3 μm, given a biologically relevant range of g. Figure 2c shows the theoretical latency of these axons if they were 10cm long, about the length of motor callosal fibers. The figure shows that using d=2μm in the numerical simulation lead to callosal delays around 10-20 ms. This range is close to that found in electrophysiological studies (85–89), and even shorter when measured with response-time differences (33,90). For the following sections, we will use an axon diameter of 2μm microns. It is noteworthy to mention that while choosing a smaller axon diameter creates unreasonably long delays, it also increases the effect of g on the conduction time estimate (because the velocity is much smaller).

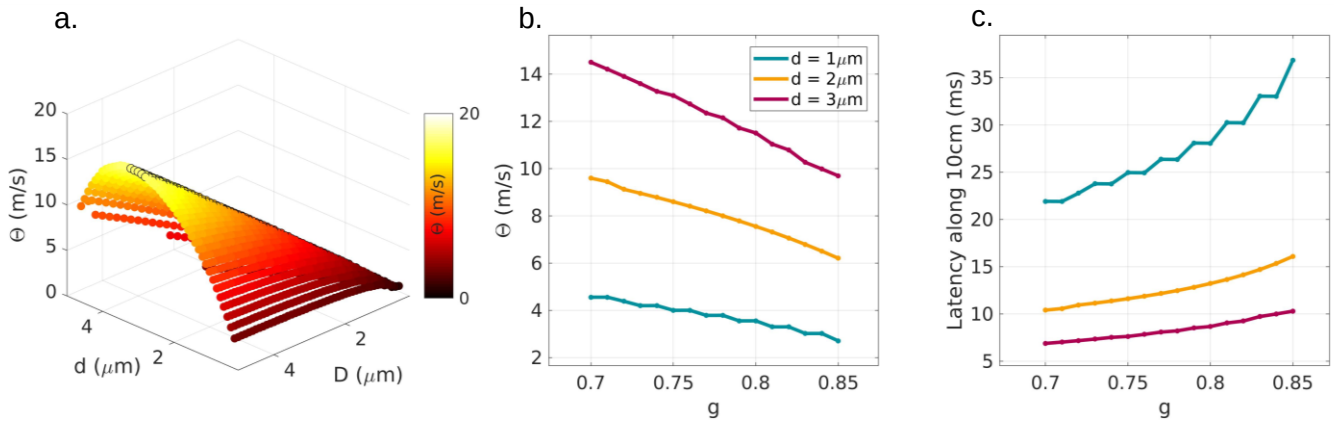

Figure 2: Simulating conduction. A numerical simulation (40) for estimating the conduction velocity. **a**. Conduction velocity plotted as a function of axon (d) and fiber (axon + myelin) diameter (D), peak velocity can be found around g-ratio=0.6, marked with black circles. **b**. Conduction velocity as a function of a small biological range of g, plotted for three values of axon diameter (1,2,3 μm) **c**. Conduction delay for the velocities in **b** and a distance of 10cm. The delays for the larger axons are around 5-20ms, similar to inter hemispheric transfer time measured with EEG.

Methods

Having established a framework aimed at relating qMRI data, and a biophysical model of conduction, we tested whether it would provide sound estimates of conduction latency along white matter fibers. We calculated the predicted latency of signal transfer along callosal fibers in two subject groups that are expected to have variance between them.

3.1 Participants

The MRI measurements were performed on 20 young adults (aged 27 ± 2.1 years, 9 females), and 17 older adults (aged 67.4 ± 6 years, 5 females). The Helsinki Ethics Committee of Hadassah Hospital, Jerusalem, Israel approved the experimental procedure. Written informed consent was obtained from each participant prior to the procedure.

3.2. MRI Acquisition.

Data was collected on a 3T Siemens MAGNETOM Skyra scanner equipped with a 32-channel head receive-only coil at the ELSC neuroimaging unit at the Hebrew University.

Quantitative T1, & MTV mapping: 3D Spoiled gradient (Flash) echo images were acquired with different flip angles (α = 4°, 10°, 20° and 30°), TE/TR = 3.34/19 ms. The scan resolution was 1 mm isotropic. For calibration, we acquired an additional spin-echo inversion recovery scan with an echo-planar imaging (EPI) read-out (SEIR-epi). This scan was done with a slab-inversion pulse and spatial-spectral fat suppression. For SEIR-epi, the TE/TR was 49/2920 ms. TI were 200, 400, 1,200, and 2,400 ms. We used

2-mm in-plane resolution with a slice thickness of 3 mm. The EPI readout was performed using 2× acceleration.

Diffusion mapping: Whole-brain DTI measurements were performed using a diffusion-weighted spin-echo EPI sequence with isotropic 1.5-mm resolution. Diffusion weighting gradients were applied along 64 directions and the strength of the diffusion weighting was set to $b = 2000\ s/mm^2$ (TE/TR=95.80/6,000 ms, G=45 mT/m, δ=32.25 ms, Δ=52.02 ms). The data include eight non-diffusion-weighted images ($b = 0$). In addition, we collected non-diffusion-weighted images in 6 directions with reversed phase-encode blips.

Anatomical images: 3D magnetization prepared rapid gradient echo (MP-RAGE) scans were acquired for 24 of the subjects (14 from the younger subjects, 10 from the older subjects). The scan resolution was 1 mm isotropic, the TE/TR was 2.98/2300 ms. Magnetization Prepared 2 Rapid Acquisition Gradient Echoes (MP2RAGE) scans were acquired for the rest of the subjects. The scan resolution was 1 mm isotropic, the TE/TR was 2.98/5000 ms.

3.3 Estimation of qMRI parameters.

Quantitative MTV & T1 mapping: Whole-brain MTV and T1 maps, together with bias correction maps of B1+ and B1-, were computed as described in (69,91). Voxels in which the B1+ inhomogeneities were extrapolated and not interpolated were removed from the MTV and T1 maps. The analysis pipeline for producing unbiased T1 and MTV maps is an open-source MATLAB code (available at https://github.com/mezera/mrQ).

Diffusion parameter estimation: Diffusion analysis was done using the FSL toolbox (92); Susceptibility and eddy current induced distortions were corrected using the reverse phase-encode data, with the eddy and topup commands (93,94). The corrected, unwarped data were aligned to the imaging space of the MTV map using FSL's Flirt rigid-body alignment (95,96). Diffusion tensor indices (FA, MD) maps were calculated from the aligned data using the dtifit command. Furthermore, the data was fit with the Neurite Orientation and Dispersion Diffusion Imaging (NODDI) model using the AMICO toolbox (54,97). One older subject was removed from further analysis since the unwarping pipeline was not successful in aligning the diffusion volumes, and one young subject was removed because the diffusion data was corrupt.

g-ratio: In the corpus callosum, the g-ratio was calculated with the following formula, using 2 different measurements: $g = \sqrt{1 - MVF/FVF}$. MVF was estimated using MTV (27,28), or MTsat (65). The FVF was derived either from the isotropic and intracellular volume fraction estimated from NODDI (21).

Tractography: We performed whole-brain anatomically constrained tractography using the mrTrix software (72). The white matter tracts in corpus callosum were then segmented using the Automated Fiber Quantification (AFQ) toolbox (71). We used this software to track three major callosal tracts connecting the two hemispheres: occipital,

motor, and anterior-frontal. We used the AFQ software to sample g along the the tract core, and used code from the vistasoft git repository to estimate a median g value for each streamline. One young subject and one old subject were removed from the analysis due to extremely sparse tractography results in the occipital cortex.

3.4. Latency estimation:

To test whether we predict a delay in callosal conduction time with age we first calculate the mean of the g-weighted MRI measurement along the three callosal tracts. The mean was calculated over the 20 medial nodes of the tract/streamline (for more details on the effect of the choice of node number see supplementary material). We incorporate the mean g values in the simulation to estimate conduction velocity along the different fiber groups. The latency of each tract was calculated by dividing the tract length by its velocity. Software for the analysis in this study can be found at GitHub [link].

Finally, we used the calculated latency of each streamline to simulate an LFP signal for each fiber tract. The simulation was adapted from the analysis in (75). The LFP is simulated as the sum of the time-integrated input of a population of neurons. Each neuron receives its input from one streamline. This input is modeled as a delta function of the corresponding latency of the streamline, with additive Gaussian noise. Finally, to allow for a comparison between tracts that differ in the number of streamlines, the signal is normalized to have a peak amplitude of 1 [units]. The simulated LFP signal has a large peak similar to an event related potential (ERP), and we extracted the peak time and the ERP width.

4. Results

To test whether the g-weighted MRI measurement can be incorporated in our framework for estimating white matter conduction *in vivo*, we first evaluated the g values in the corpus callosum of younger and older subjects. Fig. 3a shows the average g over the 20 medial nodes of the tract core, for each age group and fiber tract. We find that older subjects have higher g values compared with younger subjects only in the motor callosal tract ($p = 0.028, t = -1.987, df = 27.3$, uncorrected for the three comparisons) . We also found difference between the callosal regions. However, this difference is highly affected by the distance from the mid-sagittal plane (supplementary fig 1).

We incorporated the g-weighted measurements in the simulation to calculate conduction velocities fig 3b). The simulations (fig 2b) reveal the dependence of the conduction velocity on g-ratio, (given a fixed axon diameter). However, because we find only small to no significant difference in g as a function of age, we do not find significant differences between the conduction velocity of the different age groups, in any callosal tract. Next, we combined the velocity with the fiber tract lengths (fig 3c), to calculate conduction time (fig 3d). We found no significant differences between the predicted latencies of younger and older subjects, in all areas. This result could be expected from the data, as the differences that exist in the conduction velocity are small, and they are cancelled by the small (but not significant) differences in fiber length.

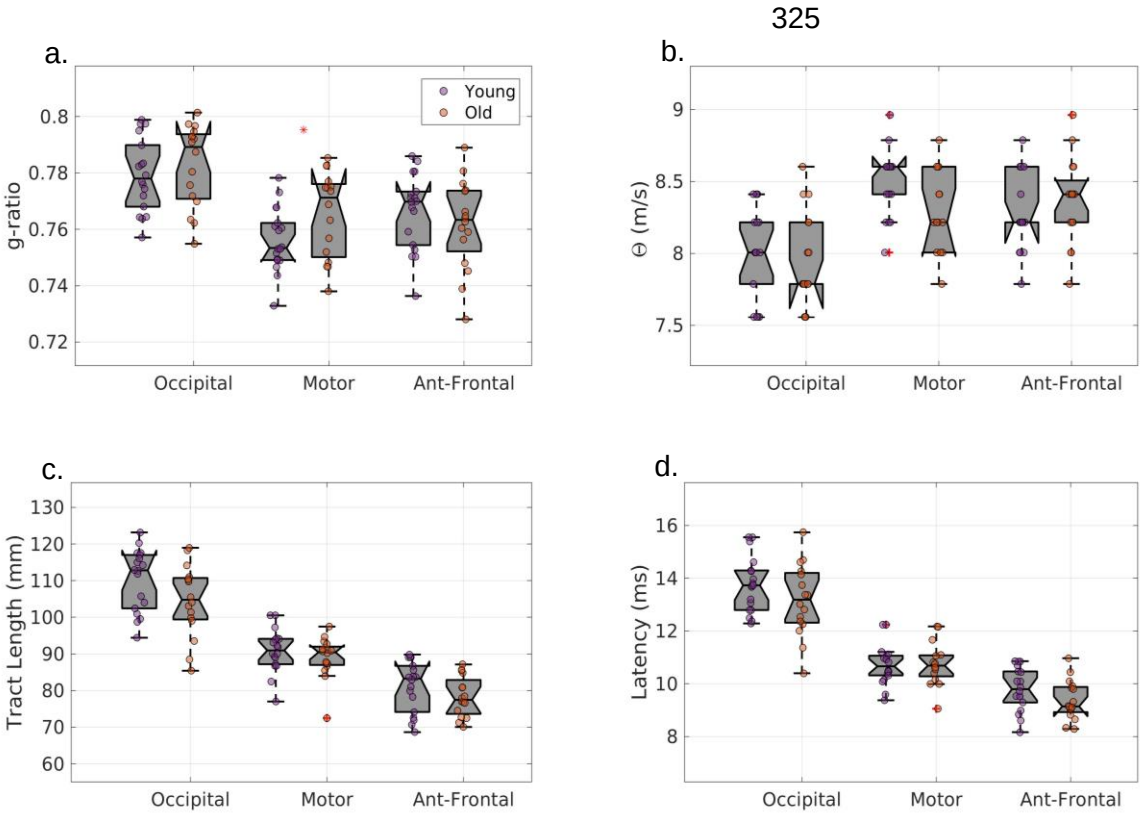

Figure 3: predicting conduction velocity and latency. a. g-ratio calculated with MTV and NODDI, showing a difference between young (purple) and old (orange) subjects, in the motor callosal region ($p = 0.028, t = -1.987$). These values were used to calculate the conduction velocity of an axon with a diameter of $2\mu\mathrm{m}$, using the numerical simulation (**b)** The model does not capture all of the differences in the g-ratio and does not show significant differences between the subject groups. The tracts' length (**c**) was used to calculate the conduction delay given the velocity (**d**).

Finally, we used the tractography streamlines to predict more conduction properties. We treated each streamline as separate representative of underlying axonal properties (instead of taking the tract core's properties to reflect a single value for all streamlines). This sampling approach creates a distribution of g values. Each streamline has its own length and g-ratio, thereby resulting in a distribution of estimated latencies. As is for the core (Fig. 3), g was sampled along the 20 medial nodes of each streamline, and the median of this sample was used. The distribution of latencies can be used for simulation of an LFP signal (shown in Fig. 4a). The peak time of the LFP is highly correlated with the latency calculated using the tract core ($R^2 = 0.91$), but it is not identical as it is sensitive to the variance across the tract Fig. 4b). Comparing the latencies between the age groups (Fig. 4c), we found no significant difference in the predicted latencies of any callosal tract.

The LFP analysis also allows us to compare the variance in the data using the signal width. Figure 4d shows the comparison of the full-width half-maximum of the simulated

LFP signal. Interestingly, this comparison of ERP width between younger and older subjects also reveals a significant difference with age in the callosal fibers connecting the occipital cortices ($p = 0.048, t = -1.76, df = 20.7$, uncorrected for the three comparisons), suggesting a higher variance within subject.

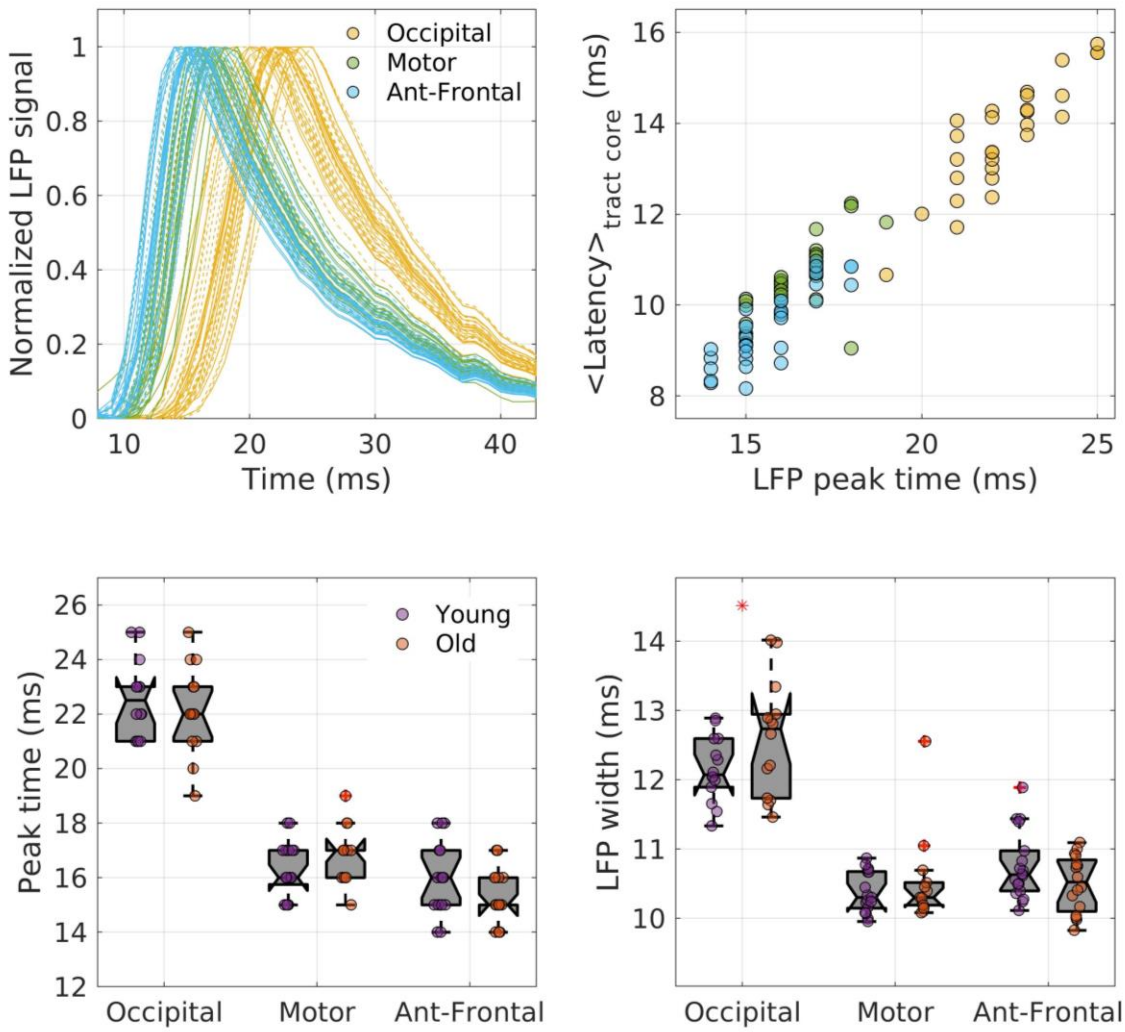

Figure 4: LFP estimates. The g-ratio and length of each streamline was used to calculate the conduction latency. The distribution of latencies for each tract was then used to simulate an LFP signal. **a**. The LFP for young (solid line) and old (dashed line) in the three fiber tracts. **b**. A comparison of the LFP peak time with the mean latency of the tract core. The values are not identical but the overall variance is maintained. Group comparison of the LFP peak time (**c**) and width (**d**) reveal different effects than those calculated with the core. The LFP width of older subjects is significantly larger in the occipital tract ($p = 0.048, t = -1.75$).

Discussion

In this study we provide a biophysical framework which relates qMRI measurements to white matter signal conduction, in an attempt to provide a link between structure features of axons and electrophysiology. We examined a recent model and investigated its approximation in a biologically relevant parameter space. As proof of concept, we then used this framework to estimate conduction changes with age in the corpus callosum of healthy human subjects. We found little to no significant difference between the young and old subject in the g-weighted measurement, nor did we find a difference in conduction estimates in the occipital frontal and motor callosal fibers.

The biophysical interpretation of the qMRI measurements relates them to properties of signal conduction along a myelinated axon. That is, estimating conduction velocity as a function of axon properties (axonal diameter, myelin thickness, and fiber length). There are other models that could have been used here. For example, given that the conduction velocity is indeed mostly affected by the geometric characteristics of the internode (rather than the node), one can reduce the conduction velocity of the axon to the conduction velocity of the internode. Assuming a semi-infinite cylinder, the conduction velocity is a function of the membrane time constant (τ) and length constant (λ) (98,99) $\theta = 2\lambda/\tau$. This solution describes unmyelinated axons better than myelinated ones, but it is convenient since it doesn't require a full simulation of the axon propagation. Different models will produce different predictions of conduction latency, but unless one chooses a model that is based on a very different set of assumptions of the axon biophysics, we do not expect it will lead to a great difference in the results.

The biophysical model is relying on structural parameters that are not available *in vivo*. We chose empirically based values, and found that it indeed produces conduction latencies which are close to those found in the literature (85,86,88,89). A second consequence of choosing a certain axon diameter (and internode length), is that it changes the effect of g-ratio on the conduction velocity. The lower the axon diameter, the less the g-ratio will affect the velocity prediction. Thus, when calculating the latency (rather than velocity), choosing a small axon diameter will weight the tract lengths more strongly.

When applying a biophysical model to MRI data, it is necessary to extract summary statistics of the microstructure parameters. One possibility is to use the voxels in a certain region (e.g. their mean). To sample white matter pathways, it is advantageous to rely on the tractography results, and either use the tract core values, or obtain the characteristic value for each streamline. While the tract core values are probably less susceptible to partial volume effects, using the streamlines allows an interesting and potentially informative sampling of the space.

Using the streamlines as a way to estimate a distribution of axonal values, is a very coarse reduction of the anatomy. Whether or not it is valid depends on the homogeneity of the axons in space within a fiber tract. Future testing is needed to decide if ERP characteristics such as latency or width are helpful when interpreting the structural MRI

data. To our knowledge, there is not enough evidence today to determine whether it is helpful to use such analysis. Nevertheless, in our data, the LFP analysis predicts group differences in the width of the ERP, which is not available when using the tract core values. The difference in ERP width suggests that the LFP simulation captures somewhat different information in the data, than using the tract core values.

We did not find any difference in conduction estimates for the callosal fibers tested here. The existing literature on callosal delays does suggest an elongation of signal transfer time with age (33,34). There are several possible explanations for this discrepancy. First, given that there is an increase in inter-hemispheric transfer time (IHTT) with age, it is possible that the increase is a result of cortical processing and not changes in white matter conduction. Second, as previously discussed (27), the myelin measure used here (MTV) is sensitive, but not specific to myelin. Therefore, as the tissue undergoes changes in composition with age, it is possible that our g-weighted measure is becoming less specific to myelin (i.e., effected by the contribution of non-myelin tissue component). On a similar note, it is possible that the single axon model is too coarse, and it might be necessary to formulate a model that considers the entire axonal populations that affects the MRI measures.

Third, the g-ratio might not capture enough of the variance that is essential for the calculation of conduction velocity. It is well established that the axon diameter is a very important determinant of conduction velocity (18,44), and this could have further implication for neural computation (100). Therefore, by fixing the axon diameter we are probably losing important information. Furthermore, studies have shown that the axon diameter distributions are related to information transfer rate and its effectiveness (101,102). Our results highlight the significance of the ongoing efforts in the qMRI community to improve and simplify *in vivo* measurement of axon diameter (e.g. 24,49,50,52,102). The internode length is another important factor that we do not have access to, and while it was found to be correlated with axon diameter, it was also shown that it is may be modulated and affect conduction velocity (78,79).

Finally, the literature describing an increase in IHTT with age, did not measure callosal conduction directly, but instead used indirect behavioral measures such as response time. Therefore, it is possible that a more direct estimation of callosal delays will reveal that they are indeed stable with age. The conduction delays can be estimated from the evoked response potential which is measured *in vivo* with methods with high temporal resolution (e.g., ECoG, EEG and MEG). The M/EEG signal represents a conglomeration of many different neural sources of activity (104). Embedded in the signal are the neural responses associated with specific sensory, cognitive, and motor events. Conduction along the corpus callosum can be accessed by presenting subjects with unilateral stimuli (tactile or visual), since such stimuli are first processed in the contralateral hemisphere, and the information is then transferred to the ipsilateral hemisphere via the corpus callosum. By measuring the same early ERP components (e.g., parietal P100) from the different hemispheres, and computing the difference between their time of occurrence,

one can estimate the IHTT – the time it took the signal to travel from one hemisphere to the other, which is an estimation of conduction delay along callosal fibers (105,106).

We tested the power of a g-weighted MRI measurement to predict conduction delays with age, and we propose that future studies would benefit from testing the framework by measuring conduction delays and structural MRI together. It should be noted, however, that the structural MRI measurements cannot be expected to fully explain the variance in the ERP latency. Of course, a higher resolution and SNR might improve the prediction. Nevertheless, predicting conduction delays can also have other limiting factors. Currently it is impossible to measure key properties, such as the internode length, that affect the conduction velocity.

The proposed framework suggests that given access to all of the white matter tissue structure parameters we might be able to predict conduction in white matter. Nevertheless, this still doesn't mean we will be able to fully predict ERP properties. The ERP latency is affected by more than the conduction in white matter. The ERP could be affected by processing time (cortical, or sensory), and potentially some properties of the skull and gyrification that could filter the signal. While the inter-individual variance of such properties is still unclear, it is unlikely to be zero. Therefore, one cannot expect to fully explain the data.

Despite the aforementioned challenges, it is important to conceptualize the relationship between structural MRI measurements and functional EEG recordings using a biophysical framework. We hope that this work can be used as a first step in bringing these two fields together in an effort to explain common sources for individual differences.

6. Summary

We provide a framework that relates MRI measurements of average microstructure features, to a single axon conduction model, in order to be able to predict white matter conduction *in vivo.* This is a critical step in the process of relating structural MRI measurements to white matter function, in a biologically relevant manner. Such models are highly reductive when we use *in vivo* measurements that are averaged over a large number of axons. Our results further suggest that using g-weighted measurement might not be enough to evaluate meaningful differences in conduction with age. It will be important to take the best available qMRI data (axon diameter estimates included), and a complementary measurement of conduction to show to what extent the models are useful. We hope that as the qMRI models develop further, this sort of study will reveal more about the human brain and behavior in healthy development, aging, and dysfunction.

Acknowledgments

This work was supported by the Ministry of Science Technology & Space, Israel (grant # 3-13395) awarded to S.B. It was also supported by the ISF Grant (no. 0399306) and the NSF/SBE-BSF Grants (NSF no. 1551330 and BSF no. 2015608) awarded to A.A.M., and a seed grant from the Eric Roland Fund for Interdisciplinary Research administered by ELSC, awarded to A.A.M. and S.B.

We thank Hiromasa Takemura, Mickey London, and Leon Deouel for their helpful comments on this manuscript.

References

1. Kanai R, Rees G. The structural basis of inter-individual differences in human behaviour and cognition. Nat Publ Gr. 2011;12.

2. Zatorre RJ, Fields RD, Johansen-Berg H. Plasticity in gray and white: neuroimaging changes in brain structure during learning. Nat Neurosci. 2012;15(4):528–36.

3. Douglas Fields R. A new mechanism of nervous system plasticity: activity-dependent myelination. Nat Publ Gr. 2015;16(12):756.

4. Moeller K, Willmes K, Klein E. A review on functional and structural brain connectivity in numerical cognition. Front Hum Neurosci. Frontiers; 2015;9:227.

5. Nagy Z, Westerberg H, Klingberg T. Maturation of white matter is associated with the development of cognitive functions during childhood. J Cogn Neurosci. 2004;16(7):1227–33.

6. Yeatman JD, Wandell B a, Mezer A a. Lifespan maturation and degeneration of human brain white matter. Nat Commun. 2014;5:4932.

7. Fields RD. White matter matters. Sci Am. 2008;298(3):42–9.

8. Compston A, Coles A. Multiple sclerosis. Lancet. 2008;372(9648):1502–17.

9. Sokol S, Moskowitz A, Towle VL. Age-related changes in the latency of the visual evoked potential: influence of check size 1. Electroencephalogr Clin Neurophysiol. 1981;51:559–62.

10. Reed TE, Vernon PA, Johnson AM. Sex difference in brain nerve conduction velocity in normal humans. Neuropsychologia. 2004;42:1709–14.

11. Polman CH, Reingold SC, Edan G, Filippi M, Hartung H-P, Kappos L, et al. Diagnostic criteria for multiple sclerosis: 2005 revisions to the “McDonald Criteria.” Ann Neurol. 2005;58(6):840–6.

12. Assaf Y, Pasternak O. Diffusion Tensor Imaging (DTI)-based White Matter Mapping in Brain Research: A Review. J Mol Neurosci. 2008;34(1):51–61.

13. Horsfield M a., Jones DK. Applications of diffusion-weighted and diffusion tensor MRI to white matter diseases - A review. NMR Biomed. 2002;15(7–8):570–7.

14. Gunning-Dixon FM, Brickman AM, Cheng JC, Alexopoulos GS. Aging of cerebral white matter: a review of MRI findings. Int J Geriatr Psychiatry. 2009;24(2):109–17.

15. Pumphrey RJ, Young JZ. The rates of conduction of nerve fibres of various diameters in cephalopods. J Exp Biol. 1938;15(4):453–66.

16. Michailov G V, Sereda MW, Brinkmann BG, Fischer TM, Haug B, Birchmeier C, et al. Axonal Neuregulin-1 Regulates Myelin Sheath Thickness. Science (80-).

2004;304(5671):700–3.

17. Cullheim S. Relations between cell body size, axon diameter and axon conduction velocity of cat sciatic α-motoneurons stained with horseradish peroxidase. Neurosci Lett. 1978;8(1):17–20.

18. Rushton WAH. A theory of the effects of fibre size in medullated nerve. J Physiol. 1951;115(1):101–22.

19. Chomiak T, Hu B. What is the optimal value of the g-ratio for myelinated fibers in the rat CNS? A theoretical approach. PLoS One. 2009;4(11):e7754.

20. Stikov N, Campbell JSW, Stroh T, Lavelée M, Frey S, Novek J, et al. Quantitative analysis of the myelin g -ratio from electron microscopy images of the macaque corpus callosum. Data Br. 2015;4:368–73.

21. Stikov N, Campbell JSW, Stroh T, Lavelée M, Frey S, Novek J, et al. In vivo histology of the myelin g-ratio with magnetic resonance imaging. Neuroimage. 2015;118:397–405.

22. Guy J, Ellis EA, Kelley K, Hope GM. Spectra of G ratio, myelin sheath thickness, and axon and fiber diameter in the guinea pig optic nerve. J Comp Neurol. 1989;287(4):446–54.

23. Arnett H, Mason J, Marino M. TNFα promotes proliferation of oligodendrocyte progenitors and remyelination. Nat Neurosci. 2001;4(11):1116.

24. Pesaresi M, Soon-Shiong R, French L, D.R. Kaplan, Miller FD, Paus T. Axon diameter and axonal transport: In vivo and in vitro effects of androgens. Neuroimage. 2015;115:191–201.

25. Stikov N, Perry ML, Mezer A, Rykhlevskaia E, Wandell B a., Pauly john m., et al. Bound Pool Fractions Complement Diffusion Measures to Describe White Matter Micro and Macrostructure. Neuroimage. 2012;29(6):997–1003.

26. Dean DC, O'Muircheartaigh J, Dirks H, Travers BG, Adluru N, Alexander AL, et al. Mapping an index of the myelin g-ratio in infants using magnetic resonance imaging. Neuroimage. 2016;132:225–37.

27. Berman S, West KL, Does MD, Yeatman JD, Mezer AA. Evaluating g-ratio weighted changes in the corpus callosum as a function of age and sex. Neuroimage. 2018;182:304–13.

28. Duval T, McNab JA, Setsompop K, Witzel T, Schneider T, Huang SY, et al. In vivo mapping of human spinal cord microstructure at 300mT/m. Neuroimage. 2015;118:494–507.

29. Mohammadi S, Carey D, Dick F, Diedrichsen J, Sereno MI, Reisert M, et al. Whole-Brain In-vivo Measurements of the Axonal G-Ratio in a Group of 37 Healthy Volunteers. 2015;9:441.

30. Caminiti R, Ghaziri H, Galuske R, Hof PR, Innocenti GM. Evolution amplified processing with temporally dispersed slow neuronal connectivity in primates. Proc Natl Acad Sci U S A. 2009;106(46):19551–6.

31. Westerhausen R, Kreuder F, Woerner W, Huster RJ, Smit CM, Schweiger E, et al. Interhemispheric transfer time and structural properties of the corpus callosum. Neurosci Lett. 2006;409(2):140–5.

32. Horowitz A, Barazany D, Tavor I, Bernstein M, Yovel G, Assaf Y. In vivo correlation between axon diameter and conduction velocity in the human brain. Brain Struct Funct. 2014;220(3):1777–88.

33. Jeeves MA, Moes P. Interhemispheric transfer time differences related to aging and gender. Neuropsychologia. Pergamon; 1996;34(7):627–36.

34. Bellis TJ, Wilber LA. Effects of Aging and Gender on Interhemispheric Function. J Speech Lang Hear Res. 2001;44(2):246.

35. Peters A, Moss MB, Sethares C. Effects of aging on myelinated nerve fibers in monkey primary visual cortex. J Comp Neurol. 2000;419(3):364–76.

36. Sandell JH, Peters a. Effects of age on nerve fibers in the rhesus monkey optic nerve. J Comp Neurol. 2001;429(4):541–53.

37. Waxman SG, Koscic JD, Stys P k. The Axon: Structure, Function, and Pathophysiology. Oxford University Press, Inc .; 1995.

38. Moore JW, Joyner RW, Brill MH, Waxman SD, Najar-Joa M. Simulations of conduction in uniform myelinated fibers. Relative sensitivity to changes in nodal and internodal parameters. Biophys J. 1978;21(2):147–60.

39. Haltert JA, Clark JW. A Distributed-parameter Model of the Myelinated Nerve Fiber. J theor BioL. 1991;148:345–82.

40. Basser PJ. Cable equation for a myelinated axon derived from its microstructure. Med Biol Eng Comput. 1993;31(1):S87–92.

41. Debanne D, Campanac E, Bialowas A, Carlier E, Alcaraz G. Axon physiology. Physiol Rev. 2011;91(2):555–602.

42. Bakiri Y, Káradóttir R, Cossell L, Attwell D. Morphological and electrical properties of oligodendrocytes in the white matter of the corpus callosum and cerebellum. J Physiol. 2011;589(3):559–73.

43. Goldman L, Albus JS. Computation of impulse conduction in myelinated fibers; theoretical basis of the velocity-diameter relation. Biophys J. Elsevier; 1968;8(5):596–607.

44. Waxman SG. Determinants of conduction velocity in myelinated nerve fibers. Muscle Nerve. 1980;3(2):141–50.

45. Brill MH, Waxman SG, Moore JW, Joyner RW. Conduction velocity and spike configuration in myelinated fibres: computed dependence on internode distance. J Neurol Neurosurg Psychiatry. 1977;40(8):769–74.

46. Thomas P., Youl B, Pellisier JF, Huston S, Manson A, Passage E, et al. Correlation of reduction in nerve conduction velocity with varying levels of expression of human peripheral myelin protein 22 (PMP22) in a transgenic mouse

model of of demyelinating neuropathy. Electroencephalography and Clinical Neurophysiology. 1997. 12-13 p.

47. Lorena Arancibia-Cá rcamo I, Ford MC, Cossell L, Ishida K, Tohyama K, Attwell D. Node of Ranvier length as a potential regulator of myelinated axon conduction speed. Elife. 2017;6:e23329.

48. Alexander DC, Dyrby TB, Nilsson M, Zhang H. Imaging brain microstructure with diffusion MRI: practicality and applications. NMR Biomed. 2017;e3841.

49. Drobnjak I, Zhang H, Ianuş A, Kaden E, Alexander DC. PGSE, OGSE, and sensitivity to axon diameter in diffusion MRI: Insight from a simulation study. Magn Reson Med. 2016;75(2):688–700.

50. Novikov DS, Fieremans E, Jespersen SN, Kiselev VG. Quantifying brain microstructure with diffusion MRI: Theory and parameter estimation. arXiv Prepr. 2016;arXiv:1612.

51. Assaf Y, Blumenfeld-Katzir T. AxCaliber: a method for measuring axon diameter distribution from diffusion MRI. Magn Reson Med An Off J Int Soc Magn Reson Med. 2008;59(6):1347–54.

52. Benjamini D, Komlosh ME, Holtzclaw LA, Nevo U, Basser PJ. White matter microstructure from nonparametric axon diameter distribution mapping. Neuroimage. 2016;135:333–44.

53. Xu J, Li H, Harkins KD, Jiang X, Xie J, Kang H, et al. Mapping mean axon diameter and axonal volume fraction by MRI using temporal diffusion spectroscopy. Neuroimage. 2014;103:10–9.

54. Zhang H, Schneider T, Wheeler-Kingshott CA, Alexander DC. NODDI: Practical in vivo neurite orientation dispersion and density imaging of the human brain. Neuroimage. 2012;61(4):1000–16.

55. Alexander DC, Hubbard PL, Hall MG, Moore EA, Ptito M, Parker GJM, et al. Orientationally invariant indices of axon diameter and density from diffusion MRI. Neuroimage. 2010;52(4):1374–89.

56. Reisert M, Mader I, Umarova R, Maier S, Tebartz van Elst L, Kiselev VG. Fiber density estimation from single q-shell diffusion imaging by tensor divergence. Neuroimage. 2013;77:166–76.

57. Campbell JSW, Leppert IR, Narayanan S, Duval T, Cohen-Adad J, Pike GB, et al. Promise and pitfalls of g-ratio estimation with MRI. 2017;182:80–96.

58. Basser PJ, Jones DK. Diffusion-tensor MRI: theory, experimental design and data analysis - a technical review. NMR Biomed. 2002;15(7–8):456–67.

59. Deoni SCL, Matthews L, Kolind SH. One component? Two components? Three? The effect of including a nonexchanging “free” water component in multicomponent driven equilibrium single pulse observation of T 1 and T 2. Magn Reson Med. 2013;70(1):147–54.

60. Mackay A, Whittall K, Adler J, Li D, Paty D, Graeb D. In vivo visualization of

myelin water in brain by magnetic resonance. Magn Reson Med. 1994;31(6):673–7.

61. Meyers SM, Kolind SH, MacKay AL. Simultaneous measurement of total water content and myelin water fraction in brain at 3T using a T2 relaxation based method. Magn Reson Imaging. 2017;37:187–94.

62. West KL, Kelm ND, Carson RP, Gochberg DF, Ess KC, Does MD. Myelin volume fraction imaging with MRI. Neuroimage. 2016;182:511–21.

63. Nam Y, Lee J, Hwang D, Kim D-H. Improved estimation of myelin water fraction using complex model fitting. Neuroimage. 2015;116:214–21.

64. Jung W, Lee J, Shin H-G, Nam Y, Zhang H, Oh S-H, et al. Whole brain g-ratio mapping using myelin water imaging (MWI) and neurite orientation dispersion and density imaging (NODDI). Neuroimage. Academic Press; 2017 Sep 27;182:379–88.

65. Helms G, Dathe H, Kallenberg K, Dechent P. High-resolution maps of magnetization transfer with inherent correction for RF inhomogeneity and T 1 relaxation obtained from 3D FLASH MRI. Magn Reson Med. 2008;60(6):1396–407.

66. Sled JG, Pike GB. Quantitative imaging of magnetization transfer exchange and relaxation properties in vivo using MRI. Magn Reson Med. 2001;46(5):923–31.

67. Yarnykh VL. Actual flip-angle imaging in the pulsed steady state: A method for rapid three-dimensional mapping of the transmitted radiofrequency field. Magn Reson Med. 2007;57(1):192–200.

68. Cercignani M, Giulietti G, Dowell NG, Gabel M, Broad R, Leigh PN, et al. Characterizing axonal myelination within the healthy population: a tract-by-tract mapping of effects of age and gender on the fiber g-ratio. Neurobiol Aging. 2017;49:109–18.

69. Mezer A, Rokem A, Berman S, Hastie T, Wandell BA. Evaluating quantitative proton-density-mapping methods. Hum Brain Mapp. 2016;37(10):3623–35.

70. Ellerbrock I, Mohammadi S. Four in vivo g -ratio-weighted imaging methods: Comparability and repeatability at the group level. Hum Brain Mapp. 2018;39(1):24–41.

71. Yeatman JD, Dougherty RF, Myall NJ, Wandell B a., Feldman HM. Tract Profiles of White Matter Properties: Automating Fiber-Tract Quantification. PLoS One. 2012;7(11).

72. Tournier J-D, Calamante F, Connelly A. MRtrix: Diffusion tractography in crossing fiber regions. Int J Imaging Syst Technol. 2012;22(1):53–66.

73. Smith SM, Jenkinson M, Johansen-Berg H, Rueckert D, Nichols TE, Mackay CE, et al. Tract-based spatial statistics: Voxelwise analysis of multi-subject diffusion data. Neuroimage. 2006;31(4):1487–505.

74. De Santis S, Drakesmith M, Bells S, Assaf Y, Jones DK. Why diffusion tensor MRI

does well only some of the time: Variance and covariance of white matter tissue microstructure attributes in the living human brain. Neuroimage. 2014;89:35–44.

75. Hermes D, Nguyen M, Winawer J. Neuronal synchrony and the relation between the blood-oxygen-level dependent response and the local field potential. Kohn A, editor. PLOS Biol. 2017;15(7):e2001461.

76. Eyal G, Verhoog MB, Testa-Silva G, Deitcher Y, Lodder JC, Benavides-Piccione R, et al. Unique membrane properties and enhanced signal processing in human neocortical neurons. Elife. 2016;5:e16553.

77. Young KM, Psachoulia K, Tripathi RB, Dunn S-J, Cossell L, Attwell D, et al. Oligodendrocyte Dynamics in the Healthy Adult CNS: Evidence for Myelin Remodeling. Neuron. 2013;77(5):873–85.

78. Friede RL. The Significance of Internode Length for Saltatory Conduction: Looking Back at the Age of 90. J Neuropathol Exp Neurol. 2017;76(4):258–9.

79. Etxeberria A, Hokanson KC, Dao DQ, Mayoral SR, Mei F, Redmond SA, et al. Dynamic Modulation of Myelination in Response to Visual Stimuli Alters Optic Nerve Conduction Velocity. J Neurosci. 2016;36(26):6937–48.

80. Hursh JB. Conduction velocity and diameter of nerve fibers. Am J Physiol. 1939;127:131–9.

81. Friede RL, Bischhausen R. How are sheath dimensions affected by axon caliber and internode length? Brain Res. 1982;235(2):335–50.

82. Aboitiz F, Scheibel a B, Fisher RS, Zaidel E. Fiber composition of the human corpus callosum. Brain Res. 1992;598(1–2):143–53.

83. Ibrahim ' M, Butt AM, Berry M. Relationship between myelin sheath diameter and internodal length in axons of the anterior medullary velum of the adult rat. J Neurol Sci. 1995;133(1):119–27.

84. West KL, Kelm ND, Carson RP, Does MD. A revised model for estimating g-ratio from MRI. Neuroimage. Elsevier B.V.; 2015;

85. Moes PE, Brown WS, Minnema MT. Individual differences in interhemispheric transfer time (IHTT) as measured by event related potentials. Neuropsychologia. 2007;45(11):2626–30.

86. Whitford TJ, Kubicki M, Ghorashi S, Schneiderman JS, Hawley KJ, McCarley RW, et al. Predicting inter-hemispheric transfer time from the diffusion properties of the corpus callosum in healthy individuals and schizophrenia patients: A combined ERP and DTI study. Neuroimage. 2011;54(3):2318–29.

87. Patston LLM, Kirk IJ, Rolfe MHS, Corballis MC, Tippett LJ. The unusual symmetry of musicians: Musicians have equilateral interhemispheric transfer for visual information. Neuropsychologia. 2007;45(9):2059–65.

88. Terada K, Umeoka S, Usui N, Baba K, Usui K, Fujitani S, et al. Uneven interhemispheric connections between left and right primary sensori-motor areas. Hum Brain Mapp. 2012;33(1):14–26.

89. Terada K, Usui N, Umeoka S, Baba K, Mihara T, Matsuda K, et al. Interhemispheric Connection of Motor Areas in Humans. J Clin Neurophysiol. 2008;25(6):351–6.

90. Marzi CA, Bisiacchi P, Nicoletti R. Is interhemispheric transfer of visuomotor information asymmetric? Evidence from a meta-analysis. Neuropsychologia. 1991;29(12):1163–77.

91. Mezer A, Yeatman JD, Stikov N, Kay KN, Cho N-J, Dougherty RF, et al. Quantifying the local tissue volume and composition in individual brains with magnetic resonance imaging. Nat Med. 2013;19(12):1667–72.

92. Jenkinson M, Beckmann CF, Behrens TEJ, Woolrich MW, Smith SM. FSL. Neuroimage. 2012;62(2):782–90.

93. Andersson JLR, Skare S, Ashburner J. How to correct susceptibility distortions in spin-echo echo-planar images: application to diffusion tensor imaging. Neuroimage. 2003;20(2):870–88.

94. Andersson JLR, Sotiropoulos SN. An integrated approach to correction for off-resonance effects and subject movement in diffusion MR imaging. Neuroimage. 2016;125:1063–78.

95. Jenkinson M, Bannister P, Brady M, Smith S. Improved optimization for the robust and accurate linear registration and motion correction of brain images. Neuroimage. 2002;17(2):825–41.

96. Jenkinson M, Smith S. A global optimisation method for robust affine registration of brain images. Med Image Anal. 2001;5(2):143–56.

97. Daducci A, Canales-Rodríguez EJ, Zhang H, Dyrby TB, Alexander DC, Thiran J-P. Accelerated Microstructure Imaging via Convex Optimization (AMICO) from diffusion MRI data. Neuroimage. 2015;105:32–44.

98. Agmon-Snir H, Segev I. Signal delay and input synchronization in passive dendritic structures. J Neurophysiol. 1993;70(5):2066–85.

99. Rall W. Core conductor theory and cable properties of neurons. Handb Physiol - Nerv Syst I. 2011;39–97.

100. Innocenti GM, CarlÃ M, Dyrby TB. Chapter15. The Diameters of Cortical Axons and Their Relevance to Neural Computing. Axons Brain Archit. 2015;317–36.

101. Perge J a, Niven J, Mugnaini E, Balasubramanian V, Sterling P. Why Do Axons Differ in Caliber? 2012;32(2):626–38.

102. Perge J a, Koch K, Miller R, Sterling P, Balasubramanian V. How the optic nerve allocates space, energy capacity, and information. J Neurosci. 2009;29(24):7917–28.

103. Fieremans E, Burcaw LM, Lee H-H, Lemberskiy G, Veraart J, Novikov DS. In vivo observation and biophysical interpretation of time-dependent diffusion in human white matter. Neuroimage. 2016;129:414–27.

104. Luck S. Ten simple rules for designing ERP experiments. Event-related potentials A methods Handb. 2005;17–32.

105. Brown WS, Jeeves MA. Bilateral visual field processing and evoked potential interhemispheric transmission time. Neuropsychologia. 1993;31(12):1267–81.

106. Fendrich R, Hutsler J, Gazzaniga M. Visual and tactile interhemispheric transfer compared with the method of Poffenberger. Exp Brain Res. 2004;158(1):67–74.

Supplementary figures

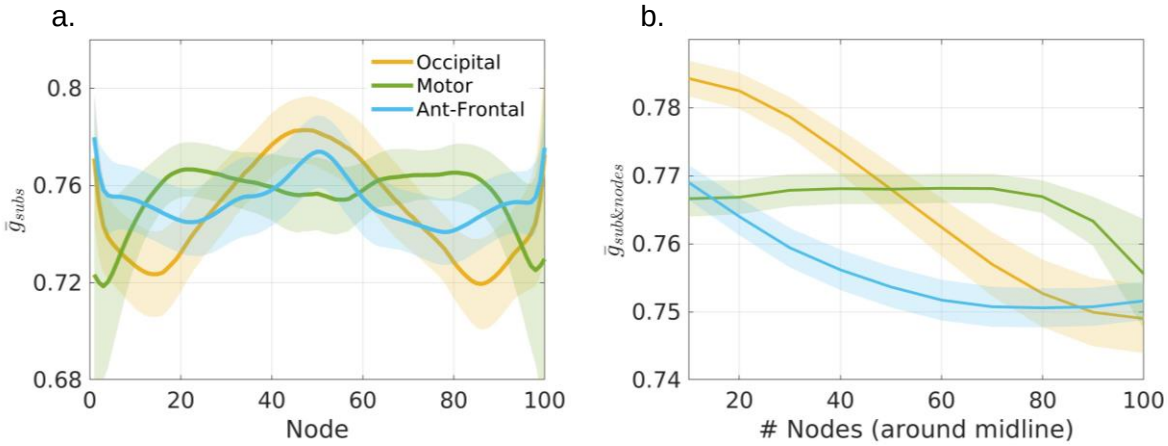

Supplementary figure 1: a. The plot shows the average g across subjects at each node along the fiber tract (100 nodes, from left to right). The shaded area represents the std at each node. The three tracts show different relationships with respect to the node location. **b.** To characterize the g of a tract, we average over several nodes. The average is plotted as a function of the number of nodes taken around the midline (node 50), from 10 nodes to the entire tract (shaded area represents STD). The relationship between the callosal tracts changes as a function of the number of nodes taken to calculate the mean.

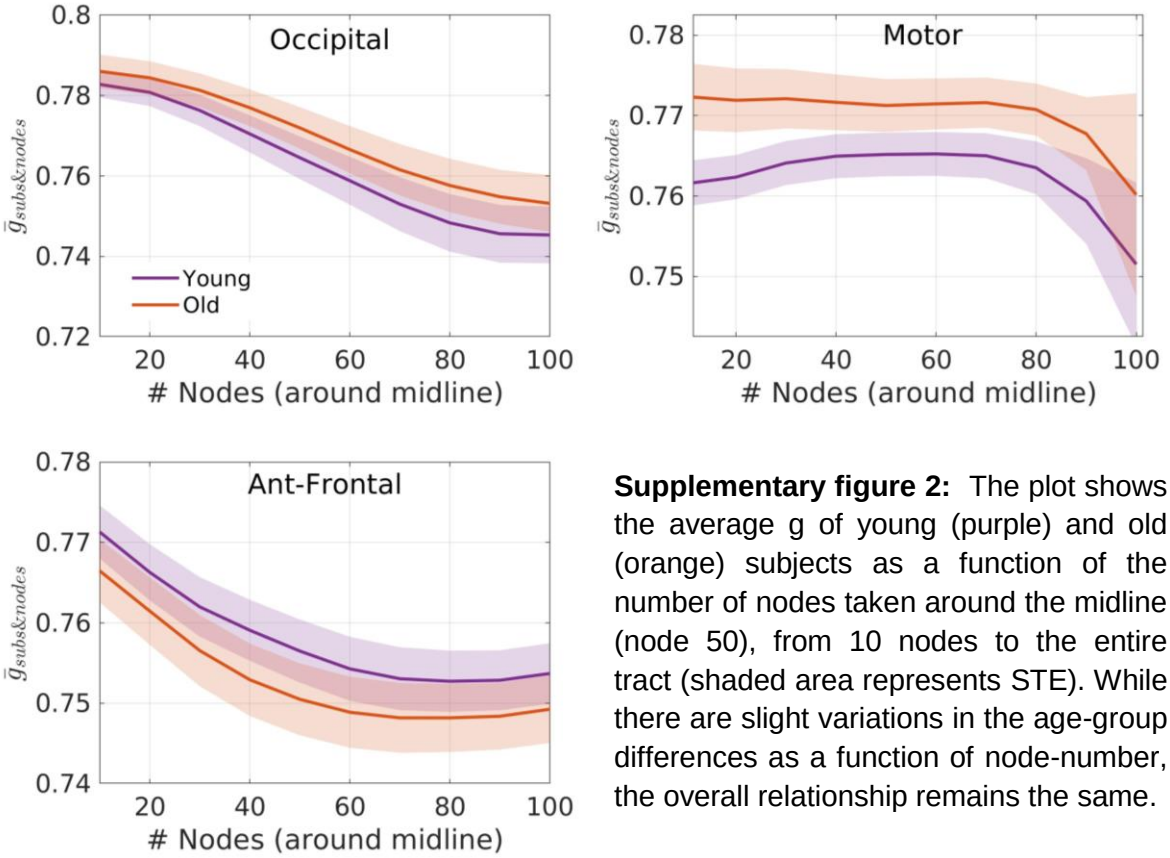

Supplementary figure 2: The plot shows the average g of young (purple) and old (orange) subjects as a function of the number of nodes taken around the midline (node 50), from 10 nodes to the entire tract (shaded area represents STE). While there are slight variations in the age-group differences as a function of node-number, the overall relationship remains the same.